Outstanding fracture toughness combines gigapascal yield strength in an N-doped heterostructured medium-entropy alloy

Xiaoru Liu [a,b,1], Shengde Zhang [a,b,1], Hao Feng [c,1], Jing Wang [a], Ping Jiang [a], Huabing Li [c], Fuping Yuan [a,b,*], Xiaolei Wu [a,b,*]

[a] State Key Laboratory of Nonlinear Mechanics, Institute of Mechanics, Chinese Academy of Sciences, Beijing 100190, China
[b] School of Engineering Science, University of Chinese Academy of Sciences, Beijing 100049, China
[c] School of Metallurgy, Northeastern University, Shenyang 110819, China

ARTICLE INFO

ABSTRACT

The superior strength and toughness balance prevails in the face-centered-cubic-structured high/medium-entropy alloys (H/MEAs) of low strength, while a gain in yield strength is normally accompanied by a sacrifice in toughness, leading to the strength and toughness trade-off particularly when yield strength increases to the gigapascal levels. Here, we showed the superior fracture toughness by heterostructuring an N-doped CrCoNi MEA having different levels of yield strength higher than 1 GPa. The fracture toughness was 91 MPa·m$^{1/2}$ at yield strength of 1.3 GPa in the heterogeneous lamella structure and 168 MPa·m$^{1/2}$ at yield strength of 1.0 GPa in the heterogeneous grain structure. The fracture toughness was attributed to forest hardening plus an extra hetero-deformation induced hardening. The pile-ups of geometrically necessary dislocations were observed to be formed at the domain boundaries to accommodate strain gradient at the plastic zone of the crack tip. The chemical short-range orders were found for the enhanced strain hardening near the crack tip by the interaction with dislocations. Moreover, a new parameter was proposed to characterize the work hardening capacity at the crack tip by the integral of hardness increment in the plastic zone which shows a linear relation-ship with the *J*-integral value during the crack initiation.

1. Introduction

The alloys of multi-principle elements, also called high/medium-entropy alloys (H/MEAs), have drawn extensive attentions due to their extraordinary mechanical properties [1–6]. In particular, the H/MEAs of face-centered-cubic-structured (FCC) single phase, such as CrCoNi MEA and FeCrMnCoNi HEA, have exhibited high fracture toughness at room temperature and even better damage tolerance at cryogenic temperature [7,8]. The excellent mechanical properties are attributed to the stable FCC matrix, high density of deformation-induced nano-twins [9–14], and chemical short-range orders (CSROs) at the atomic scale [15–22]. However, the relatively low yield strength of single FCC phase H/MEAs with coarse grains (CGs) would restrict their engineering applications. In general, elevation in strength by severe plastic deformation is inevitably accompanied by reduced toughness due to the diminished strain hardening [23–25].

A promising strategy for achieving high toughness with elevated strength is to introduce heterogeneous structure (HS) in HEAs/MEAs with single FCC phase. The HS usually consists of soft (lower strength) and hard (higher strength) domains, such as gradient structure [26–30], heterogeneous lamella structure (HLS) [31–33], and heterogeneous grain structure (HGS) [34]. During plastic deformation in HS, plastic incompatibility is generally observed near heterogeneous interfaces. As a result, geometrically necessary dislocations (GNDs) can be produced, which can promote extra strengthening and strain hardening [4,35-37]. Previous studies have extensively investigated the improved tensile properties and the corresponding deformation mechanisms induced by HS in HEAs/MEAs [4,28,34]. However, only a few reports have examined the fracture toughness of HS at the gigapascal yield strength level for other conventional alloys. For example, the fracture toughness of 316L austenitic stainless steel was observed to be enhanced at the yield strength (σ_y) of 1.0 GPa by embedded nano-twin bundles, which can inhibit void initiation in the nano-grained matrix and result in crack bridging ligaments behind the crack [38,39]. Recent reports also

---

* Corresponding authors.
  E-mail addresses: fpyuan@lnm.imech.ac.cn (F. Yuan), xlwu@imech.ac.cn (X. Wu).
[1] These authors contribute to the work equally.

indicated that high fracture toughness at σ_y ~2.0 GPa and 1.5 GPa can be achieved in the lamellar dual-phase steel [40] and the lamellar austenitic steel [33], respectively. The superior synergy of strength and toughness can be contributed to the toughening mechanisms of grain boundary delamination and transformation-induced plasticity (TRIP) effect. While, the fracture toughness for HEAs/MEAs with HS and the corresponding hardening/toughening mechanisms at the heterogeneous interfaces and at the crack tip have not been reported.

Moreover, CSROs in HEAs/MEAs also play an important role in both strengthening and strain hardening during tensile deformation, by providing strong resistance to dislocation glide [15,16,18,21,41-43]. Atomistic simulations in the CrCoNi MEA have previously exhibited the ability of CSROs to raise the activation barriers for dislocation activities, producing a significant amount of extra energy to de-trap dislocations from local CSROs [15,16]. In addition, solution strengthening is another efficient strategy to improve strength without significantly sacrificing ductility and toughness [44–51]. The addition of even a small amount of interstitials (such as carbon and nitrogen) in FCC HEAs/MEAs can significantly improve the tensile properties. The interstitials not only increase the lattice friction to dislocation motion but also interact with dislocations to change their glide pattern, resulting in higher dislocation storage and stronger strain hardening ability [48–50]. Therefore, both the CSROs and the interstitial solution strengthening are expected to enhance the fracture toughness at high strength levels in HEAs/MEAs.

Here, we propose a strategy in FCC HEAs/MEAs to provide high fracture toughness with high strength. Heterogeneous structures with gigapascal-level yield strength on an N-doped CrCoNi MEA (CrCoNiN$_{1.75}$ MEA) were designed. HLS and HGS were obtained via cold rolling and annealing at proper temperatures. The tensile and fracture toughness tests were conducted. Moreover, the corresponding crack propagation behaviors and the toughening mechanisms for the superior fracture toughness were systematically investigated by microstructural characterizations in the CrCoNiN$_{1.75}$ MEA.

2. Materials and experimental methods

2.1. Materials

The CrCoNiN$_{1.75}$ (at.%) MEA was produced from high purity elements of Cr (99.17%), Co (99.98%), and Ni (99.96%) in a pressurized induction furnace, and was melted under nitrogen pressure of 2.0 MPa. To ensure homogeneity, the ingots were homogenized at 1200 °C for 24 h, and then hot forged to 15 × 70 × 240 mm^3 plates in the temperature range of 950 °C-1200 °C. The plates were subsequently solution treated at 1150 °C for 1 h followed by water quenching. This microstructure was hereafter named as the coarse-grain (CG) counterpart. The average grain size of the CG sample was estimated to be about 14 μm (Fig. S1). The plates were cold-rolled to a final thickness of 5 mm, and these specimens were named as the cold rolling (CR) counterparts. The samples with HLS (HS$_1$) and the samples with HGS (HS$_2$) were finally obtained by annealing at a temperature of 700 °C for 30 min and 800 °C for 10 min, respectively.

2.2. Mechanical testing

The plate specimens for quasi-static tensile testing were obtained *via* electrical discharge machining. The specimen had a dog-bone shape and a gauge section of 10 × 2.5 × 1.0 mm^3. The quasi-static uniaxial tensile tests were conducted using an MTS landmark testing machine at a strain rate of 5 × 10^{-4} s^{-1} and at room temperature under displacement control. Three tensile tests were conducted for each specimen to check the repeatability of experimental data. The tensile direction was set to be parallel to the rolling direction (RD) (Fig. 1). The crack direction, the crack plane and the crack growth direction are also indicated in Fig. 1.
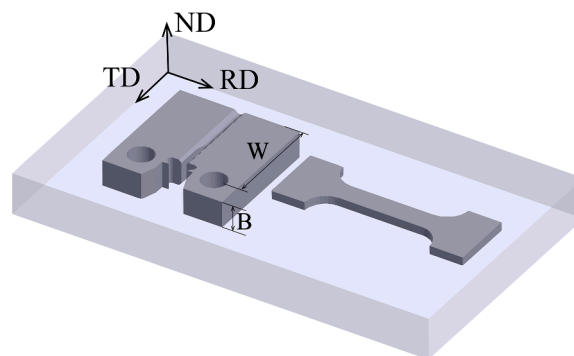

Fig. 1. Schematic illustration for preparing the tensile and fracture specimens from the plates.

For fracture toughness tests, miniaturized compact-tension (CT) specimens were cut with a thickness (B) of 4 mm, and a width (W=3B) of 12 mm. A straight-through notch was cut with a length of 5.4 mm according to the ASTM standard E1820 [52], with the crack direction perpendicular to the RD (Fig. 1). Before testing, both surfaces of all CT samples were ground and polished to clearly show the crack length. Prior to the fracture toughness measurement, fatigue pre-cracking was produced in force control with stress ratio (R) of 0.1. The length of the final pre-crack was about 6.0 mm for miniaturized CT specimens. The side grooves were also machined on both surfaces with a total thickness reduction of 0.2B to ensure a straight and sharp crack front. The fracture toughness testing was performed also on an MTS Landmark testing machine at a constant displacement loading rate of 0.3 mm/min, and the load-line displacement (LLD) was detected using an Epsilon clip-on gauge. The crack extension size and J-integral were obtained from the LLD curves, using the elastic compliance method. The elastic-plastic J-integral fracture resistance curves as a function of crack extension (J-R curves) were obtained using the procedure recommended in the ASTM standard E1820 [52]. For each state, three fracture tests were conducted and the error bars for the fracture toughness were provided.

The fracture toughness test was interrupted after peak force (F_p) with a force of about 0.8F_p for CR, HS$_1$ and HS$_2$ samples, and Vickers micro-hardness (Hv) distributions (hardness contours) around the crack tip for these tested samples on the center surface (plane-strain state) were examined with a Future-Tech ARS900 Vickers micro-hardness tester using a load of 25 gf and a dwell time of 15 s after polishing (Normal direction, ND). The hardness indentation sites along the radius direction of crack tip were separated by a distance of 0.05 to 0.2 mm.

2.3. Microstructure characterization

The microstructures were characterized using electron backscattered diffraction (EBSD) in a ZEISS Supra 55 scanning electron microscope (SEM) with an EBSD detector before deformation and after mechanical testing on the center surface. Both Schmid factors and GND density were obtained by EBSD analysis through Channel 5. The GND density can generally be reflected by the kernel average misorientation (KAM) value [53], and was measured near hetero-interfaces using high resolution EBSD maps with a step size less than 50 nm. The interface density was calculated by grain boundary orientation in a specific range. The fracture morphologies after fracture toughness testing were observed using a secondary electron detector in a Zeiss Supra 55 field emission SEM at 15 kV.

The microstructures were also examined using a transmission electron microscope (TEM, JEOL JSM-2100F) operated at 200 kV. High resolution TEM (HRTEM) and high-angle annular dark-field (HAADF) images were obtained by an aberration-corrected scanning transmission electron microscopy (STEM, FEI Titan Cubed Themis G2 300) operated at 300 kV, equipped with a Super-X energy disperse spectroscopy (EDS).

Nano beam electron diffraction (NBED) was performed under the TEM microprobe mode with an electron beam spot diameter of ~35 nm. The image was obtained using Flucam-Viewer with Sensitivity 6. The atomic-resolution EDS mapping was conducted at the count rate ranging from 180 to 500 cps and at a dwell time of 5 µs per pixel with a map size of 512 × 512 pixels. Line scan profiles were along the horizontal direction and the line profile represented the distribution of an element in a (111) plane. Geometric phase analysis (GPA) was used to calculate the strain field from high-resolution TEM images or HAADF images. A perfect crystal lattice gives rise to sharply peaked frequency Bragg spots, while the local lattice distortion would lead to the broadening of Bragg reflections. Thus, the strain mapping can be obtained by specific circular Gaussian mask on the reflection. The thin foils were thinned and polished to 40 µm thick from the sheets for TEM observation. The samples were then punched to disks with diameters of 3 mm and finally perforated in a twin-jet electropolishing using a solution of 5% perchloric acid and 95% ethanol at -31 °C with a potential of 28 V.

3. Results

3.1. Microstructure characterization before mechanical testing

Figure 2 presents the microstructural characterization of the sample with HLS (HS$_1$) after incomplete recrystallization annealing at 700 °C for 30 min. HS$_1$ consists of recrystallized grains (RGs, soft domain) and deformed grains (DGs, hard domain), as indicated by the image quality (IQ) maps of transverse direction (TD) and ND planes in Fig. 2a and b, respectively. The corresponding figure with various boundaries (low-angle grain boundaries, LAGBs; high-angle grain boundaries, HAGBs; Σ3 twin boundaries, TBs) for Fig. 2b is shown in Fig. 2c. The DGs contain lots of LAGBs (Fig. 2c). The RGs are characterized by three levels of grains with obviously different sizes: micrometer-grains (MGs, $d \geq 1$ µm, white), ultrafine-grains (UFGs, 0.25 µm $< d < 1$ µm, light purple), and nano-grains (NGs, $d \leq 0.25$ µm). The smallest NGs are marked in terms of the magnitude of the Schmid factors. The color coding in Fig. 2c will be kept the same in the following similar figures. The RGs are almost dislocation-free in Fig. 2c and do not show obvious textures in the

inverse pole figure (IPF, Fig. 2d and Fig. S2b). Obviously, bimodal grain size distribution is observed in the RGs (Fig. 2e). Specifically, two peaks of grain size distribution can be easily identified at 0.26 µm and 1.50 µm. The fraction of Cr$_2$N precipitates is about 1.1% and the average size ($\bar{d}$) is about 96 nm (Fig. S2). Figure 2f indicates that the volume fraction of DGs is 54.0% in the FCC matrix.

A complete recrystallized sample with HGS (HS$_2$) after annealing at 800 °C for 10 min is displayed in Fig. 3. The IQ maps of the TD and ND planes in Fig. 3a and b show that HS$_2$ is completely recrystallized. IPF image in Fig. 3c shows equiaxed grains and random grain orientation. The figure with various boundaries in Fig. 3d shows three levels of grains in HS$_2$. The insert of Fig. 3d shows that NGs mostly nucleate at the GBs and triple junctions of UFGs and MGs, and are surrounded by HAGBs and TBs. Fig. 3e shows the multi-modal grain size distribution with peaks at 0.15 µm, 0.67 µm, and 1.19 µm. High density TBs are shown in Fig. 3f. Moreover, some Cr$_2$N precipitates are marked in yellow in Fig. 3d. These precipitates exhibit uneven distribution and tend to precipitate preferentially at the recrystallized region. The fraction of Cr$_2$N precipitates is about 1.2% and the average size of Cr$_2$N precipitates is about 73 nm (Fig. S3). The corresponding EDS mapping with atomic-resolution in Fig. S3 shows no obvious segregation in the distribution of elements, whereas large concentration fluctuation at the atomic level is observed.

3.2. Mechanical behaviors

3.2.1. Tensile and fracture properties

The tensile properties and the J-integral-based crack resistance (J-R) curves for various samples are shown in Fig. 4. Figure 4a displays the tensile engineering stress-strain ($\sigma_e - \varepsilon_e$) curves. HS$_1$ exhibits a yield strength (σ_y) as high as 1.3 GPa, along with a uniform elongation (ε_u) of 13%. σ_y and ε_u of HS$_2$ are 1.05 GPa and 24%, respectively. Yield strength (σ_y) is determined by a linear line with the same slope as the elastic part and the 0.2% plastic strain offset. The normalized hardening rates of HS$_1$ and HS$_2$ show an upturn phenomenon in the transient range (Fig. 4b), which could be related to hetero-deformation induced (HDI) hardening [27,31,34]. In contrast, the normalized hardening rates of CR and CG decrease monotonously with increasing strain.
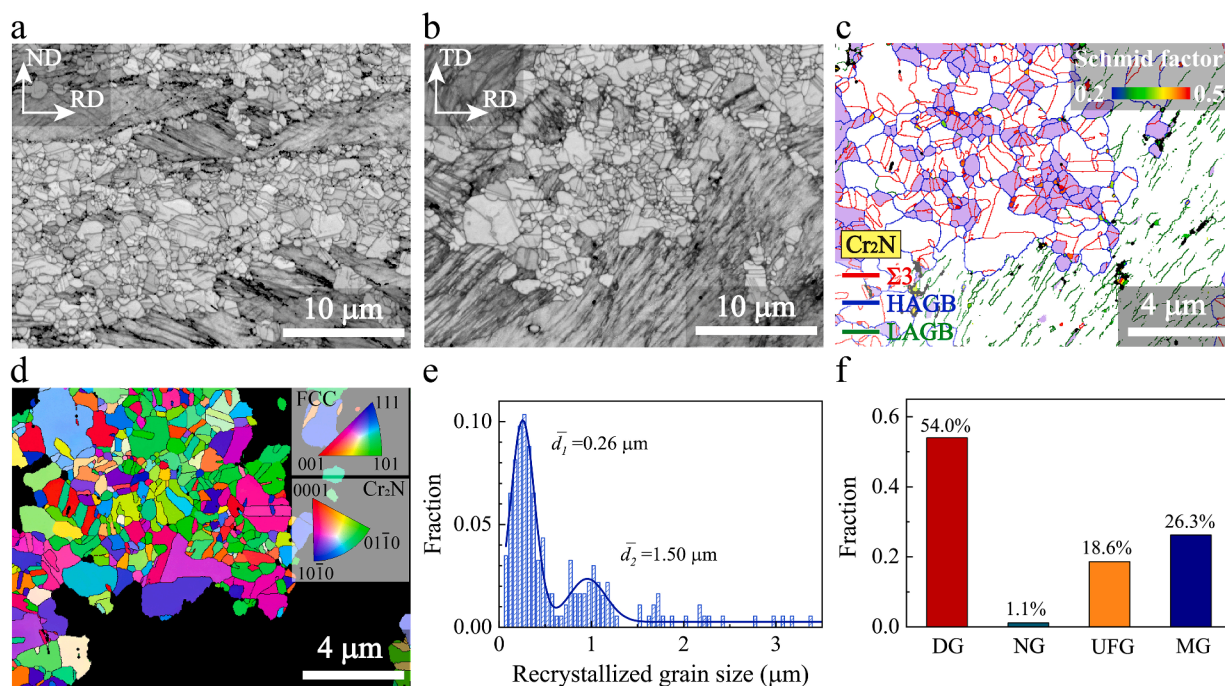

Fig. 2. The HS$_1$ sample with HLS. (a)(b) EBSD IQ maps of the TD and ND planes, respectively. (c) The corresponding enlarged figure with various boundaries for (b). (d) IPF image of RGs for (c). (e) Grain size distribution of RGs in ND plane. (f) Volume fractions of DGs, NGs, UFGs and MGs in ND plane.
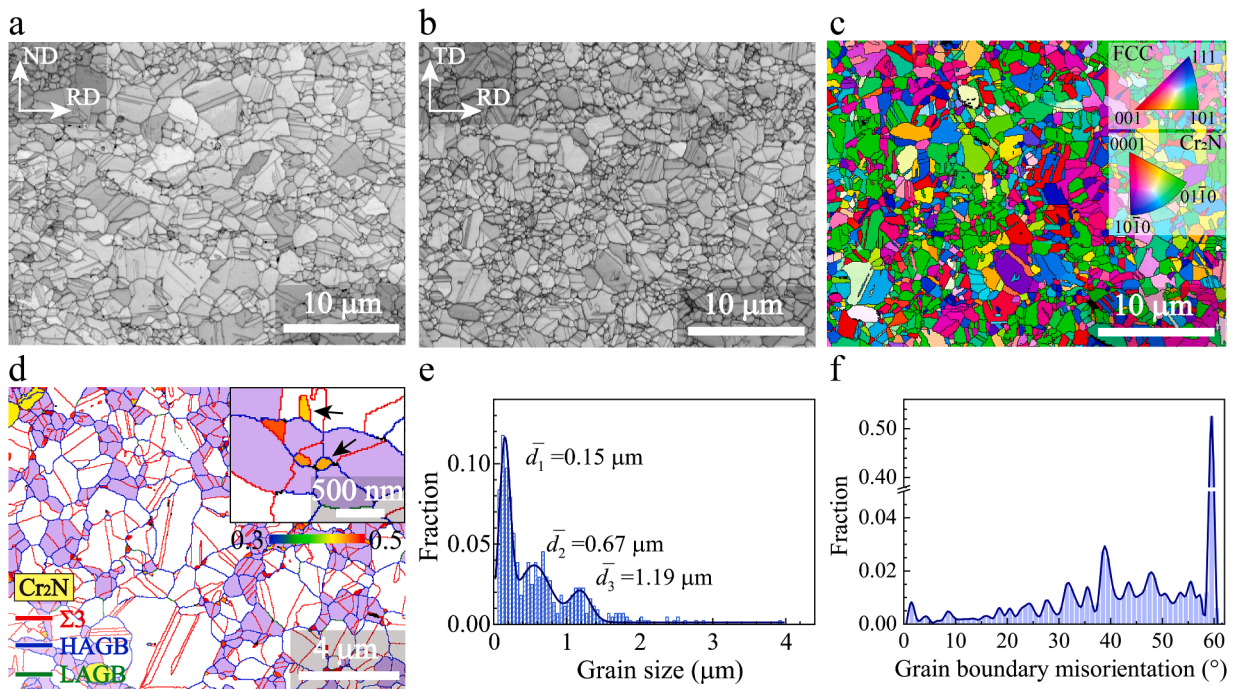
Fig. 3. The HS$_2$ sample with HGS. (a) (b) EBSD IQ maps of the TD and ND planes, respectively. (c) IPF image of (b). (d) Close-up view of (c) with various boundaries in the ND plane showing three levels of grains. (e) Grain size distribution in the ND plane. (f) Distribution of grain boundary orientation in the ND plane.
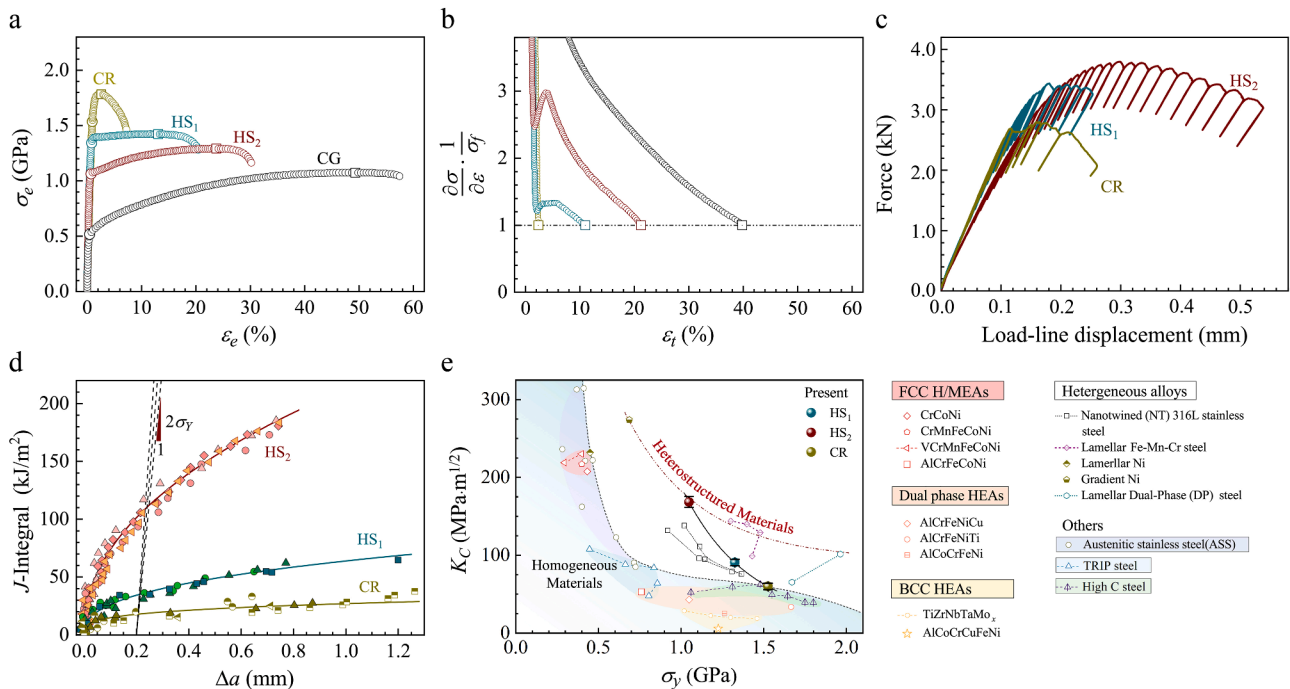

Fig. 4. Tensile and fracture toughness properties. (a) Tensile engineering stress-strain ($\sigma_e - \varepsilon_e$) curves. (b) Curves of normalized hardening rate ($1/\sigma_f \cdot \partial\sigma/\partial\varepsilon$) versus true strain ($\varepsilon_t$). (c) Curves of force as a function of load-line displacement. (d) J-R curves for the fracture toughness tests. (e) Yield strength versus fracture toughness for the present CrCoNiN$_{1.75}$ MEA, along with the data for other alloys, including HEAs/MEAs [7,8,54–60], austenitic stainless steels [33,38,61–63], TRIP steels [64, 65], Nickel [32,66], high carbon (C) steels [67], dual-phase steels [40].

Figure 4c shows the representative force versus load-line displacement curves for the HS$_1$, HS$_2$, and CR samples. The ratios of the maximum force P_{max} to P_Q (the intersected force point between the curve and the linear line with a 95% slope of the initial linear part for the curve) are larger than 1.1 due to severe crack tip plastic deformation before crack extension. Hence the direct determination of the critical

stress-intensity factor (K_{IC}) with linear-elastic plane strain conditions is invalid. Instead, elastic-plastic fracture mechanics method based on J-integral is adopted to evaluate the fracture toughness.

As shown in Fig. 4d, the J-R curves are obtained by the elastic compliance method. The J-integral value of crack initiation (J_{IC}) is determined by the intersection point of J-R curves and the 0.2 mm offset

blunting lines [52]:

$$J_Q = 2\sigma_Y \cdot \Delta a \tag{1}$$

Where σ_Y is the effective yield strength, $\sigma_Y = (\sigma_y + \sigma_u)/2$, and σ_u is the ultimate tensile strength. The J_Q value is determined to be 14 ± 2 kJ/m^2, 32 ± 3 kJ/m^2, and 112 ± 9 kJ/m^2 for the CR, HS$_1$, and HS$_2$ samples, respectively. In this work, the plane strain condition is well satisfied and J_Q can be regarded as the valid J_{IC} according to the ASTM E1820 standard [52]. Therefore, K_{IC} can be obtained from J_{IC}, using $K_J = \sqrt{(E'J_{IC})}$, where $E' = E/(1 - \nu^2)$ (E is Young's modulus, ν is Poisson's ratio). The calculated K_{IC} is determined to be 91 ± 4 MPa·m$^{1/2}$ and 168 ± 7 MPa·m$^{1/2}$ for HS$_1$ and HS$_2$, respectively.

As shown in Fig. 4e, heterogeneous CrCoNiN$_{1.75}$ MEA shows excellent synergy of yield strength and fracture toughness under high strength levels as compared to other HEAs/MEAs with homogeneous structures 57-60]. In addition, the K_{IC} of HS$_2$ at $\sigma_y \sim 1$ GPa is also higher than that of heterogeneous nano-structured 316L stainless steel at similar σ_y [38], although the heterogeneous 316L stainless steel shows a slightly higher K_{IC} than the CrCoNi MEA with homogeneous coarse-grained structure in our previous report [68]. In summary, a superior strength-toughness synergy can be achieved through the design of heterogeneous structures (Fig. 4e).

3.2.2. Micro-hardness evolution

To investigate the work hardening behavior of the plastic zone in CT samples, the micro-hardness (Hv) distributions around the crack tips for both heterogeneous structures (HS$_1$, HS$_2$) and the CR sample are characterized (Fig. 5). It shows different degrees of hardening with an enhancement of Hv as compared to those before deformation, as shown in the CR sample (Fig. 5a), the HS$_1$ sample (Fig. 5b), and the HS$_2$ sample (Fig. 5c). The average Hv after the fracture tests as a function of the distance (r) from the crack tip is displayed in Fig. 5d, in which the maximum hardness increment (ΔHv_m) and the plastic zone size (r_p) of

the CR, HS$_1$, and HS$_2$ samples are obtained. The ΔHv_m of the CR, HS$_1$, and HS$_2$ samples is determined to be 0.20, 0.25 and 0.75 GPa, respectively, and the corresponding r_p is 0.29 mm, 0.5 mm, and 1.1 mm, respectively. Obviously, the higher fracture toughness for the heterogeneous structures can be attributed to the much larger area of plastic zone around the crack tip and the much stronger strain hardening in the plastic zone.

Fracture toughness can be considered as a damage parameter that can be affected by both plastic zone size (r_p) and crack tip work hardening ability. We attempted to determine a characteristic parameter based on the micro-hardness data, and to establish a direct relationship of this parameter with fracture toughness. The Hv-r curves in Fig. 5d are fitted by polynomial. Their increments ($\Delta Hv = Hv - Hv_o$, Hv_o is the micro-hardness value before deformation) are integrated, to obtain the integral value in the plastic region (i.e., $J_{Hv} = \int_0^{r_p} Hv dr$, the colored shaded area in Fig. 5e). Interestingly, a positively linear relationship can be observed between the J_{Hv} value and the J-integral value at crack initiation (J_{IC}) (Fig. 5f). Therefore, the quantitative relationship between the work hardening behavior of the crack tip and the fracture toughness can be established.

3.3. Fracture surface morphology

The SEM fractographies of CT samples after fracture toughness tests for both heterogeneous and homogeneous structures are displayed in Fig. 6 to reveal the toughening mechanisms. Dimples are all observed in the SEM images of the fracture surface for the CR, HS$_1$ and HS$_2$ samples, indicating ductile fracture for these three structures. However, the dimple size of the CR sample is homogeneous (Fig. 6a), and the average dimple size is about 4.05 μm. Dimple sizes are heterogeneous in the HS$_1$ sample (Fig. 6b) and the HS$_2$ sample (Fig. 6c and d), including both equiaxed large dimples and small dimples. The size distributions and the
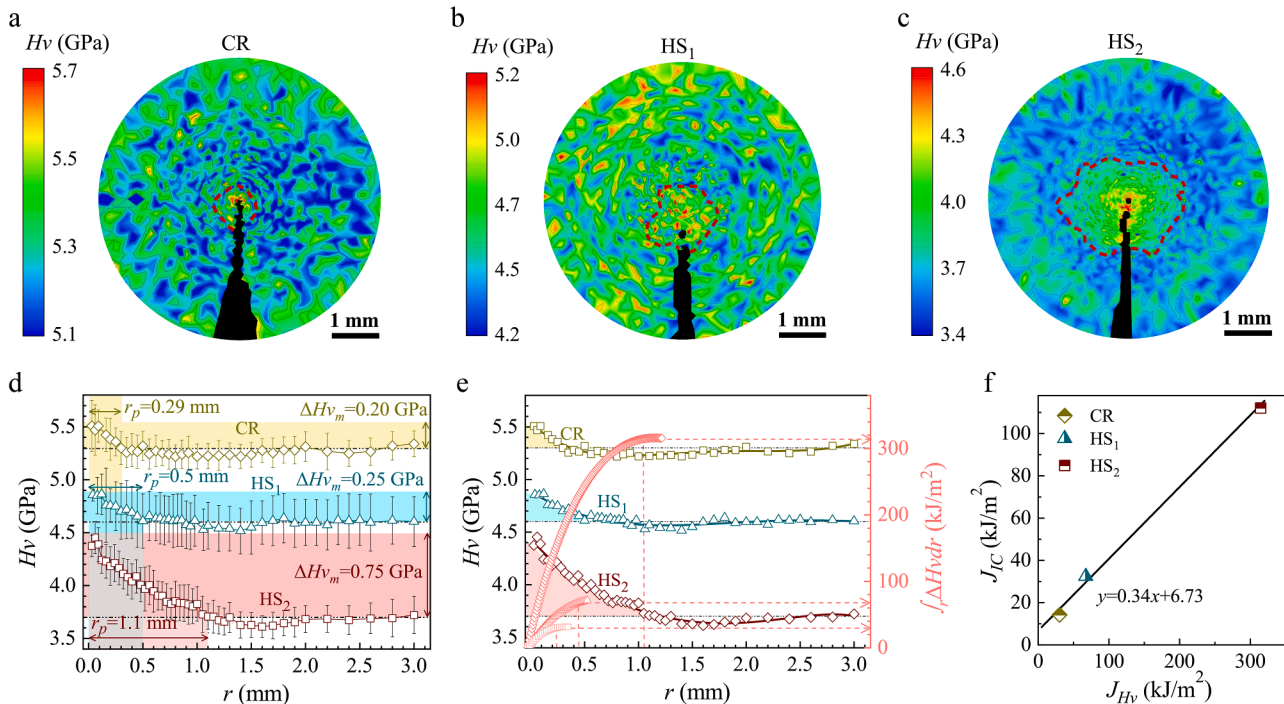

Fig. 5. Micro-hardness (Hv) distributions around the crack tips. (a)-(c) Hv contours ahead of the crack tips for the CR, HS$_1$, and HS$_2$ samples, respectively. (d) Average hardness (Hv) after fracture tests as a function of the distance (r) from the crack tip. (e) The fitting curves of Hv-r data (left y-axis) and the integral of hardness increment (ΔHv) along r (right y-axis). (f) The integral of ΔHv along r in the plastic zone (J_{Hv}, $J_{Hv} = \int_0^{r_p} \Delta Hv dr$, colored shaded area in (e)) versus J_{IC}.
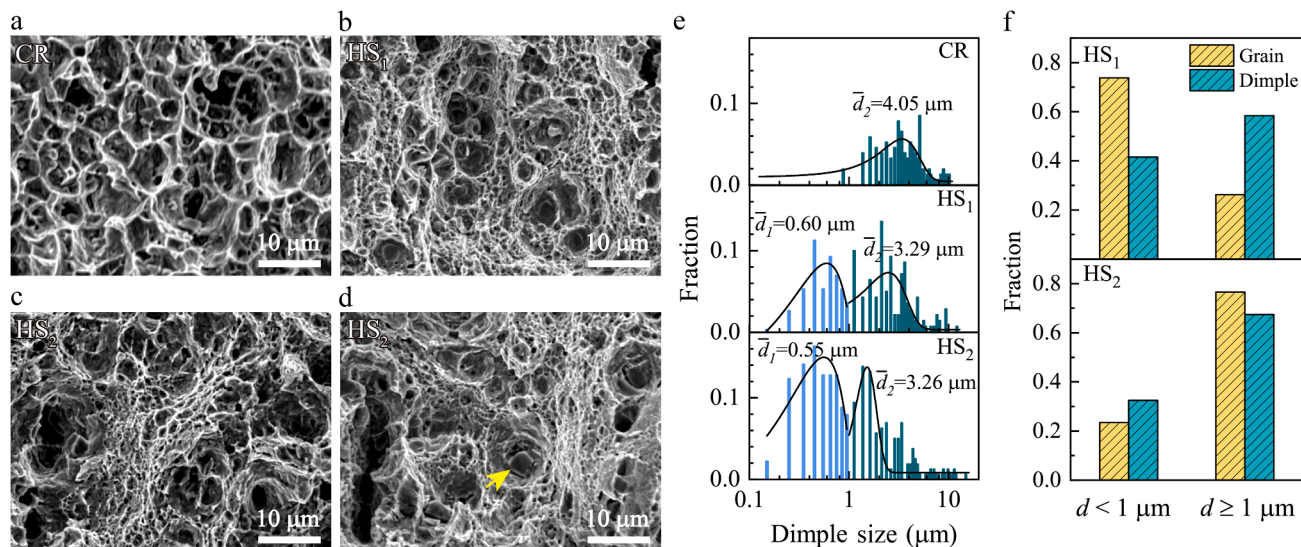
Fig. 6. Fractographies after fracture toughness testing. (a)(b) SEM images of the CR sample and the HS$_1$ sample, respectively. (c)(d) SEM images of the HS$_2$ sample. Yellow arrow: a precipitate in the dimple. (e) Distributions of dimple sizes of the CR, the HS$_1$, and the HS$_2$ samples. (f) The fractions of dimple size and grain size smaller or larger than 1 μm, for the HS$_1$ and HS$_2$ samples, respectively. (For interpretation of the references to color in this figure legend, the reader is referred to the web version of this article.)

volume fractions of large dimples ($d \geq 1$ μm) and small dimples ($d < 1$ μm) for various samples are analyzed and displayed in Fig. 6e and f. Two peaks of dimple size distributions are observed in both the HS$_1$ and HS$_2$ samples, which can be attributed to the heterogeneous grain structures in these two samples. The proportion of large dimples is consistent with that of MGs in HS$_2$ (complete recrystallization without DGs), and the proportion of large dimples is much higher than that of MGs in HS$_1$ due to high density of DGs in HS$_1$. Therefore, these small dimples are derived from NGs and UFGs, while large dimples are derived from MGs and DGs. The recrystallized MGs have strong work hardening to inhibit crack growth, and the UFGs and DGs can provide higher strength. Thus, the combination of MGs, NGs, UFGs and DGs in the heterogeneous structure can improve toughness due to the synergistic effect.

3.4. Microstructure characterization along the crack path

To illustrate the underlying toughening mechanisms for the excellent fracture toughness in the heterogeneous structures, the microstructures along the crack path and around the crack tip are characterized and displayed in Fig. 7. For the HS$_1$ sample, the propagating crack is relatively straight (Fig. 7a). The SEM image (Fig. 7b) and the IPF image (Fig. 7c) exhibit a very slender crack (as marked by the black arrow) that propagates forward quickly in DGs due to the lower work hardening capacity of DGs. However, obvious passivation is observed as the crack extends to the recrystallized region, indicating that RGs have higher work hardening and can effectively restrain the crack propagation. Close-up view of the crack tip with the boundary map (Fig. 7d) shows that Cr$_2$N precipitates (yellow zone) are the potential nucleation sites of micro-voids. The HS$_2$ sample with complete recrystallization shows a more deflective crack (Fig. 7e and f). Similar to the HS$_1$ sample, the micro-voids nucleate at the sites of Cr$_2$N precipitates (red arrows marked in Fig. 7f). Some crack branches are also observed beside the main crack, dissipating more energy. The IPF image is shown in Fig. 7g, and the corresponding close-view of the crack tip is shown in Fig. 7h. It is shown that the Cr$_2$N precipitates can be cut through by the crack propagation, and the crack tip is blunter for the HS$_2$ sample.

As indicated by the grain size distributions prior to and after fracture tests around the crack tip in Fig. 8a, grain refinement occurs along the crack path in the HS$_2$ sample. In the upper figure of Fig. 8b, the average grain size ($\bar{d}$) decreases from 0.63 μm to 0.37 μm with decreasing

distance from the crack tip, indicating grain refinement at the crack tip during deformation. The interface density ($\rho_{Interface}$) of LAGBs, HAGBs, and TBs is also calculated (Fig. 8b). At the crack tip, $\rho_{Interface}$ of LAGBs and HAGBs increases, while that of TBs decreases. The number density of NGs (grain number per μm^2) also increases significantly from 0.9 grains per μm^2 before deformation to 3.4 grains per μm^2 near the crack tip. It is reasonable to infer that smaller NGs are generated dynamically and some TBs transform into HAGBs during the fracture tests due to the interaction between dislocations and TBs, thus leading to the increasing number of NGs, which is similar to that previously reported in the CrCoNi MEA after a tensile deformation of about 20% [34].

To further explore the origin of the outstanding strain hardening ability for the heterogeneous structures, the statistical analysis of GND density for the vicinity along the crack path (within ~2 μm) is conducted for the HS$_2$ sample. Figure 9a shows the GND density map around the crack tip for the HS$_2$ sample, indicating high density GNDs are generated to coordinate deformation near hetero-interfaces. While the Cr$_2$N precipitates show a very low GND density, indicating nearly no plastic deformation in them. The poor plastic deformation capacity of the precipitates results in premature micro-void nucleation, which is consistent with the result in Fig. 7. Figure 9b1–b4 presents the close-up views of GND density maps at the positions with $r=2$, 100, and 500 μm, and prior to deformation. The density of GNDs is very high in the whole grains due to severe plastic deformation near the crack tip. While with increasing r, the GND density decreases progressively, and it can be observed more clearly that the GND density at the interfaces is higher than that in the grain interiors (Fig. 9b-2 and b-3).

The GND density distributions of NGs, UFGs, and MGs at the interfaces before and after deformation are also quantitatively calculated (Fig. 9c). The increment of the average GND density ($\bar{\rho}_{GND}$) near the HAGBs after fracture tests is more significant for MGs ($2.72 \times 10^{15}/m^2$) as compared to that of UFGs ($0.96 \times 10^{15}/m^2$). These results indicate that the abundant GNDs are produced at the interfaces to accommodate the strain gradient between MGs and UFGs due to strain incompatibility, resulting in HDI hardening [27,31,36]. In addition, GNDs at the TBs of UFGs and MGs are also observed (Fig. 9c; yellow histogram). The TBs in the MGs have a higher $\bar{\rho}_{GND}$ than that in the TBs of UFGs, which can be attributed to the larger average grain size of the MGs. Moreover, it is worth noting that the $\bar{\rho}_{GND}$ of the NGs is higher than that both in the UFGs and MGs. These observations may be related to the dynamic
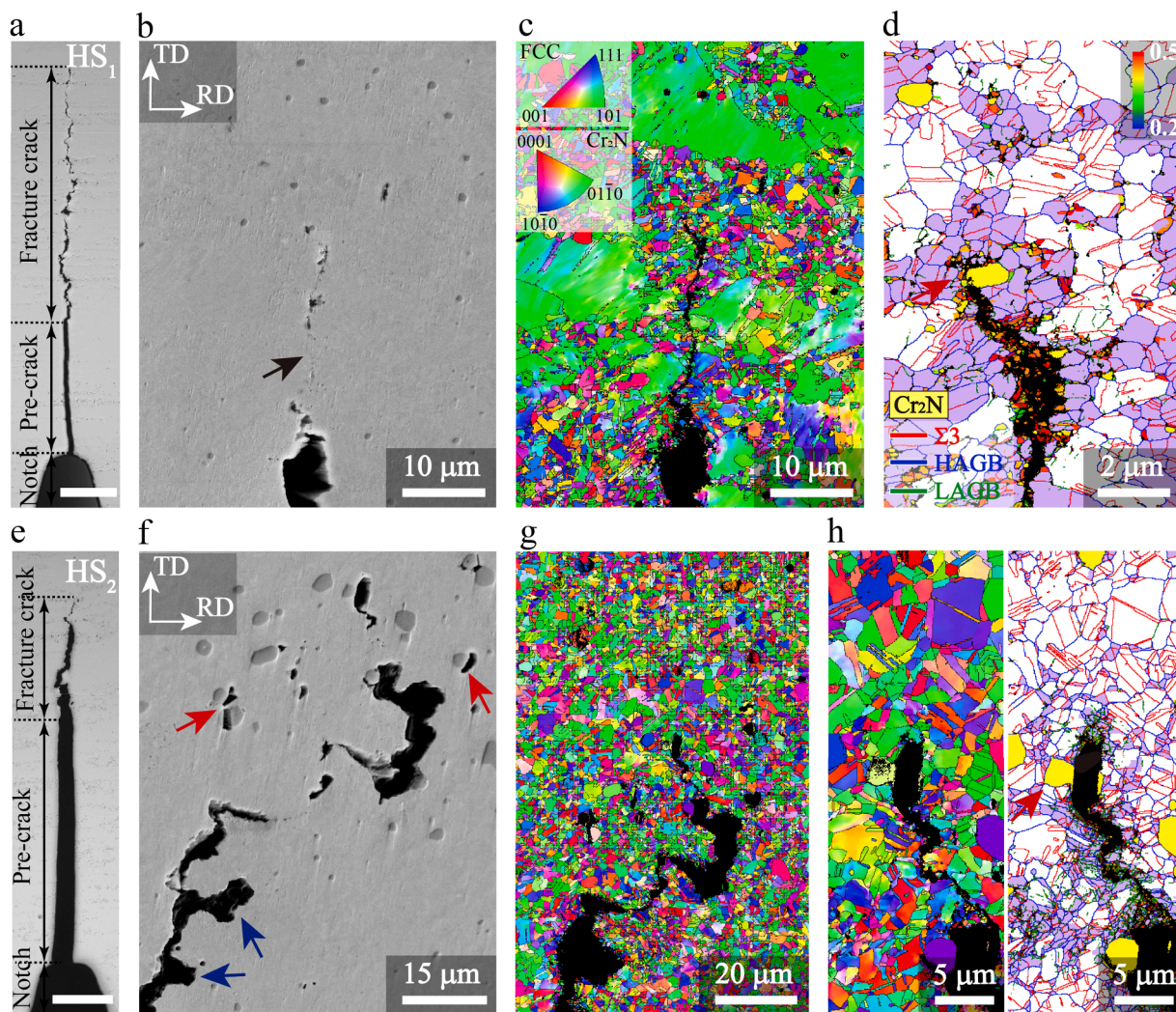
Fig. 7. Microstructure evolution along the crack path after fracture toughness testing. (a) Optical microscope (OM) image along the crack path in the HS$_1$ sample. (b) (c) SEM and IPF images around the crack tip in the HS$_1$ sample. Black arrow: slender crack in the DGs. (d) Close-up view with various boundaries around the crack tip in the HS$_1$ sample. Cr$_2$N precipitates are marked in yellow. (e) OM image along the crack path in the HS$_2$ sample. (f)(g) SEM and IPF images around the crack tip in the HS$_2$ sample. Red arrows: micro-voids nucleated at the Cr$_2$N precipitates. Blue arrows: crack branches. (h) Close-up views of IPF image and image with various boundaries around the crack tip in the HS$_2$ sample. The scale bars in (a) and (e) are 200 μm. (For interpretation of the references to color in this figure legend, the reader is referred to the web version of this article.)

generation of NGs along the GBs of MGs as reported in the CrCoNi [34]. Near the crack tip, higher stress drives the nucleation of NGs at the GBs of MGs. During this formation process, stacking faults (SFs) and dislocations are also generated inside NGs, which results in higher density of GNDs in NGs. Figure 9d shows that $\bar{\rho}_{GND}$ of the UFGs and MGs decreases monotonously with decreasing deformation degree. Notably, the enhancement of $\bar{\rho}_{GND}$ at the GBs of the MGs is larger than that of the UFGs at the crack tip, although similar values are observed in the case of lower deformation degree. This result suggests the generation of numerous GNDs at the soft domain to accommodate the deformation near the crack tip.

TEM characterization is also conducted in the plastic deformation zone of the HS$_2$ sample. Near the crack tip, severe plastic deformation is observed. Figure 10a and b shows that planar slip bands with high density dislocations pile ups near GBs in MGs. Abundant dislocations are also produced in the UFGs (Fig. 10c), indicating that UFGs also can bear some plastic deformation. At the plastic zone approximately 0.5r_c (0.5 mm) away from the crack tip, dislocations are activated and accumulated at GBs and TBs in the MGs (Fig. 10d and e). The close-up view in the inset of Fig. 10d clearly displays that dislocations are blocked by GBs. However, the planar slip dislocation band and dislocation density

are significantly reduced as compared to those near the crack tip. In addition, some deformation-induced nano-twins are observed in the grain interiors, as shown in Fig. 10f and by the selected-area electron diffraction (SAED) pattern in the inset of Fig. 10f.

3.5. The effect of CSROs on strain hardening

In the TEM characterization of the HS$_2$ sample, additional superlattice reflections were found at the position of $\frac{1}{2}\{311\}$ under the SAED pattern at [112] zone axis (Fig. S4a), which has been verified to be related to CSROs at the nanometer scale [17-20,22]. The CSROs in the HS$_2$ sample were characterized through the same method as that in VCoNi [18]. CSROs are both observed before and after deformation, and a few chemical medium-range orders (CMROs) with sizes larger than 1 nm are also observed [20] (Fig. S4 and Fig. S5). To explore the effect of CSRO/CMROs on the dislocation motion, the atomic strain field near the CSRO/CMROs is analyzed.

Figure 11a shows the HRTEM image near the crack tip of the HS$_2$ sample, in which nano-twins can be observed. Numerous dislocations (marked by "T" symbols) around TBs can be observed in a HRTEM image
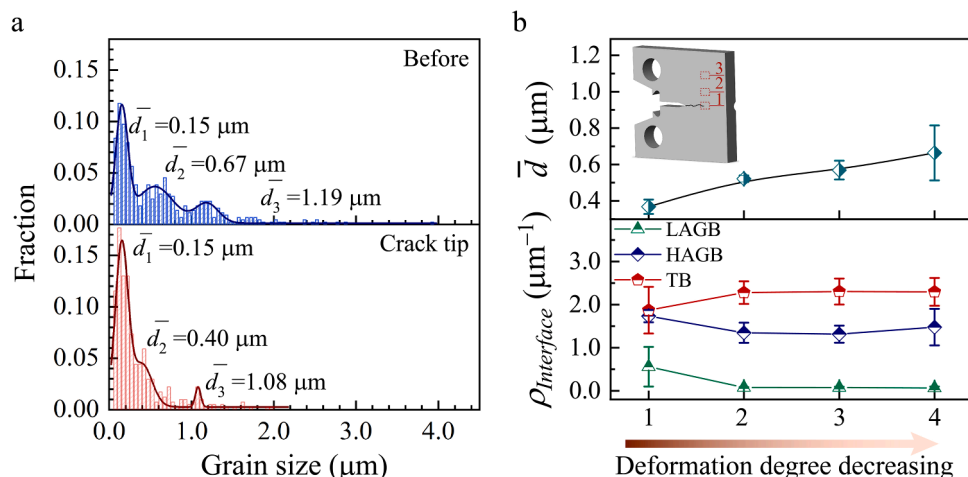
Fig. 8. Characterization of grain refinement after fracture toughness test for the HS$_2$ sample. (a) Grain size distributions prior to and after fracture tests around the crack tip. (b) The average grain size ($\overline{d}$) and the interface density ($\rho_{Interface}$) with decreasing deformation degree (increasing distance from the crack tip, r). Numbers 1-3 indicate the positions at r=2, 100 and 500 µm, number 4: prior to deformation.

with higher resolution under the [011] zone axis (Fig. 11b). The atomic strain field was analyzed by GPA in a HRTEM image with even higher resolution (Fig. 11c) [18,69,70]. The diffraction spot of FCC matrix (blue circle in the inset of Fig. 11c) is used as the reference vector for GPA, and then the map of strain contour is obtained. Figure 11d is the atomic strain field before deformation, and Fig. 11e is the atomic strain contour near the crack tip. The strain level is very low before deformation, while the strain magnitude increases significantly after deformation. In addition, the local compressive strain (blue region) and tensile strain (yellow region) are arranged alternately at atomic scale. Previous reports have shown that this strain distribution was induced by CSROs [70]. To verify this, the overlay of the atomic strain map and the inverse Fast Fourier transform (IFFT) image of CSROs by $\frac{1}{2}\{111\}$ positions under the [011] zone axis is provided in Fig. 11f [70,71]. The local tensile strain region has a good correspondence with CSROs. The EDS mapping in Fig. S6 shows that CSRO/CMROs consist of two Cr-enriched {311} planes and one sandwiched Co/Ni-enriched {311} plane. Due to similar atomic radius of Cr, Co, and Ni, the induced strain is very low before deformation. After deformation, the strain magnitude near CSROs increases significantly (Fig. 11g). More extra energy is required for dislocations to pass through CSROs due to the obstruction of CSROs, which changes the strain field near CSROs.

In the local region A of Fig. 11g, significant tensile and compressive strains with higher strain level are observed. In order to find out the formation mechanism of strain distribution at the region A, the atomic strain field with the [112] zone axis and the corresponding EDS mapping were analyzed. Figure 12a is the HAADF lattice image of FCC matrix, and Fig. 12b is the overlapped IFFT images of CSROs and FCC matrix, using extra diffuse reflections at $\frac{1}{2}\{\overline{3}11\}$ (yellow circle in the inset of Fig. 12a) and FCC diffraction spots [18,22]. The GPA strain map is also obtained using two FCC diffraction spots (blue circles in the inset of Fig. 12a) (Fig. 12c). The strain region similar to region A of Fig. 11g is found and enlarged in Fig. 12d, in which significant local tensile and compressive strains can be observed. The intensity distribution of the {111} plane of the FCC lattice (shown by the dashed line) at this position is shown in Fig. 12e, from which the spacing between adjacent atoms could be determined. The lattice on the line is found to have severe distortion. The points "2" and "3" have significant extrusion, with a spacing of 1.2 Å, which is less than the spacing of the adjacent atoms (1.5 Å). This extrusion causes a large compression deformation between "2" and "3", corresponding to the blue band in the GPA strain map. The distribution of elements is also investigated, as shown by the EDS mapping of Cr and N elements in Fig. 12f. Point "2" is occupied by Cr

atom, while an adjacent interstitial point is occupied by N atom. This arrangement should cause significant local tensile strain. Moreover, CSROs are present in this region (Fig. 12b). Therefore, the lattice near the CSROs is believed to have a large distortion through the pinning and interaction of dislocations during deformation. When a dislocation passes through a local CSRO, more energy and greater driving force are required to cross the energy barrier, which provides extra strengthening and strain hardening for better fracture toughness [16].

4. Discussion

A superior fracture toughness is found in the CrCoNiN$_{1.75}$ MEA with heterogeneous structure in Fig. 4e, compared with other alloys at a similar yield strength ($\sigma_y \sim 1$ GPa). The underlying strengthening/ toughening mechanisms responsible for the excellent strength-toughness synergy are discussed here.

4.1. Hardening mechanisms in heterogeneous structures

For metallic materials, excellent fracture toughness can be attributed to two major classes of toughening mechanisms, as summarized by Ritchie [23,25] — intrinsic and extrinsic toughening mechanisms. Intrinsic toughening is relevant to the resistance of crack initiation and small growth ahead of crack, which mainly depends on work hardening capacity. While for extrinsic toughening, the applied force is shielded in the crack wake during the crack growth stage by crack deflection, crack bridging [38,39], or grain-boundary delamination [33,40]. Extrinsic toughening is generally applicable to ceramics, bone structure, or other brittle materials by improving load capacity and toughness [25]. It has been proven to be effective to obtain outstanding toughness in austenitic steels [33,38] and dual-phase steel [40] by introducing both intrinsic and extrinsic toughening mechanisms. The intrinsic toughening is more important for improving crack initiation fracture toughness (K_{IC}) during fracture process, while intrinsic toughening mechanisms (i.e., hardening capacity) become limited at high yield strength level.

Multiple mechanisms are operated simultaneously for the present CrCoNiN$_{1.75}$ MEA with HGS. First, HGS provides a long-range hardening from the HDI stress. HGS has been previously designed in the CrCoNi MEA [34], and the enhancement of strength-ductility combination is obtained, which can be attributed to the persistent HDI hardening by reinforced heterogeneous structure during tensile deformation in the low SF energy (SFE) alloys [34]. An upturn of Θ at true strain ranging from 2 to 4% in the HS$_1$ and HS$_2$ samples is also observed, which is a typical phenomenon of strain hardening response in the initial stage for
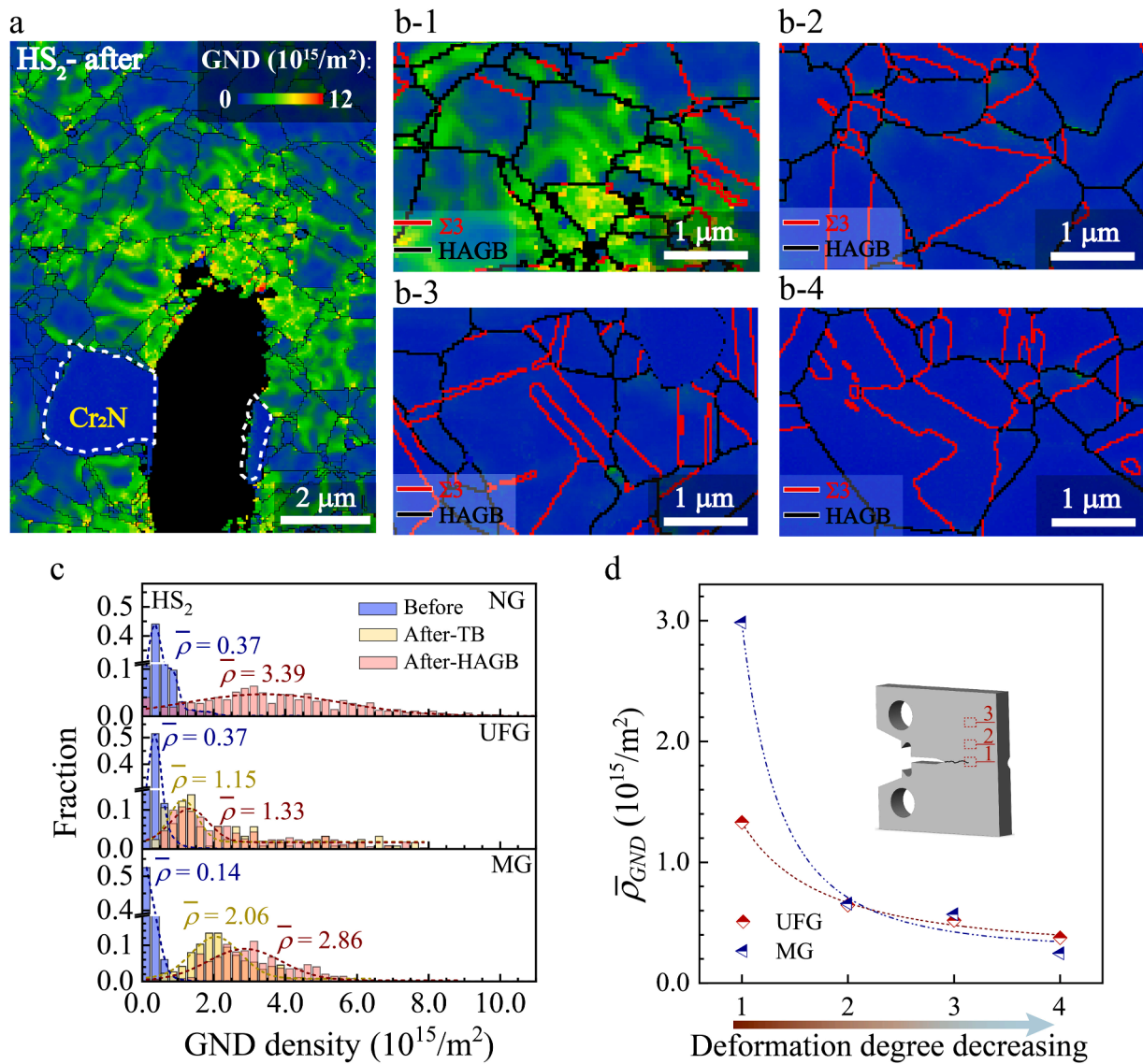
Fig. 9. GND density evolution during the fracture testing for the HS$_2$ samples. (a) The GND map at the crack tip. (b-) Close-up views of GND density maps at r=2, 100, and 500 µm and before deformation, respectively. (c) Distributions of GND density at GBs and TBs prior to and after deformation in NGs, UFGs, and MGs around the crack tip, respectively. (d) Average GND density ($\overline{\rho}_{GND}$) of UFGs and MGs at GBs as a function of decreasing deformation degree.

heterogeneous structures [27,29,31,34]. The results in Fig. 9 show that the GBs of MGs have a much higher $\overline{\rho}_{GND}$ (2.86 × 10^{15} /m^2) than that in the GBs of UFGs (1.33 × 10^{15}/m^2) near the crack tip. This indicates that MGs carry more plastic strain, relative to UFGs, inducing high-density GNDs at the crack tip in the HS$_2$ sample. These GNDs may interact with mobile dislocations to increase the density of mobile dislocations in varying grains [27,30,31], which is accompanied by strong HDI stress and hardening. By this way, the plastic deformation ability of the plastic zone is enhanced, and the initiation and propagation of cracks are refrained.

Second, the CSRO/CMROs in the structure provide significant strengthening and hardening effects. These CSRO/CMROs with nanometer size are stable even after deformation, with a volume fraction of ~3.5% (Fig. S5). Through the corresponding GPA analysis (Figs. 11 and 12), it is found that CSROs produce serious lattice distortion in the FCC matrix for inhibiting the movement of the dislocations. The energy expense would be increased when a dislocation passes through a local CSRO, resulting in stronger strain hardening in the plastic zone of the HS$_2$ sample [16]. In addition, the fraction of Cr$_2$N is measured at ~ 1.2% by EBSD, indicating that about 0.14 wt. % (0.58 at.%) of nitrogen

is concentrated in the precipitates, and the remaining 1.17 at.% of nitrogen is in the matrix (Assuming that the density is uniform in the alloy). Stronger effect of solid-solution hardening would be achieved in the N-doped MEA due to the increasing lattice distortion [46–48]. Thus, both CSROs and severe lattice distortion provide strong resistance to dislocation motion, and are expected to effectively improve the toughness.

Third, grain refinement is also observed near the crack path (Fig. 8), resulting in strain hardening due to the so-called dynamic Hall-Petch effect [32,72]. Moreover, the $\rho_{Interface}$ of TBs decreases, while $\rho_{Interface}$ of HAGBs and LAGBs increases slightly after deformation. Thus, it can be concluded that TBs lose their coherency and grain refinement happens after deformation, which leads to the increase of UFGs and NGs. This dynamic grain refinement can be attributed to the low SFE, and has also been observed in the CrCoNi MEA under both quasi-static tension and dynamic shear loading [34,72]. Hence, grain refinement is one of the origins of the high strain hardening at the crack tip.
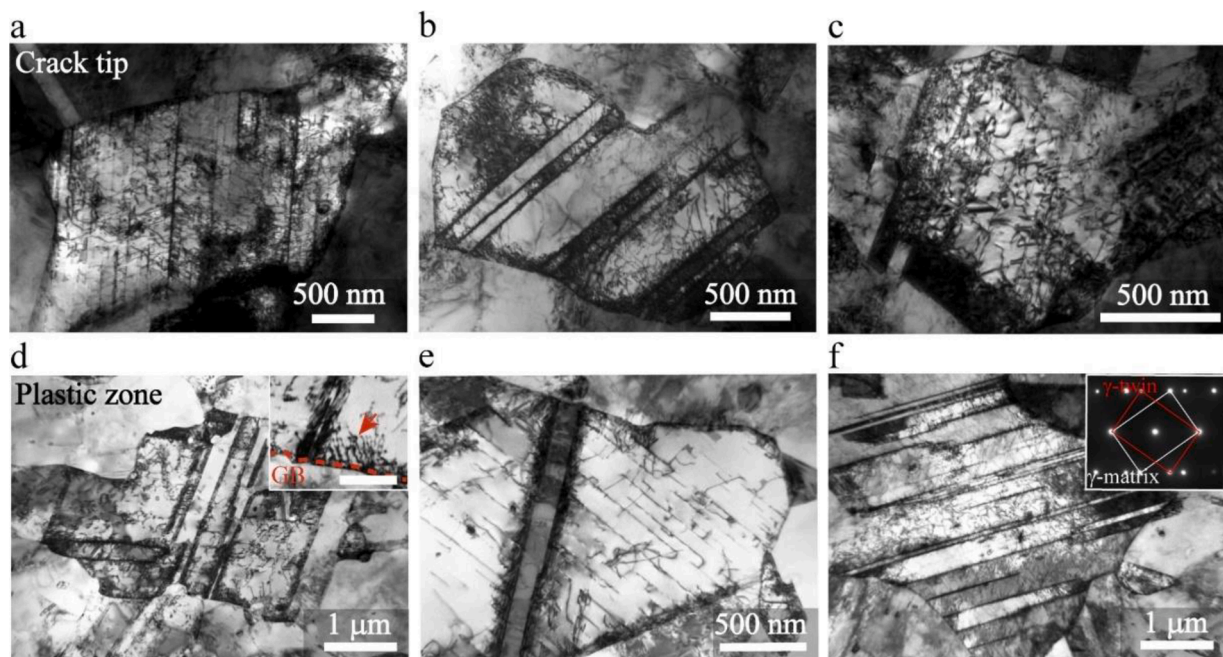
Fig. 10. TEM images characterizing the deformation mechanism of the HS$_2$ sample after the fracture toughness test. (a)-(c) TEM bright field image at the crack tip. (d)-(f) TEM bright field image in the plastic area with approximately $0.5r_c$ (0.5 mm) away from the crack tip. The scale bar in the inset of (d) is 300 nm.
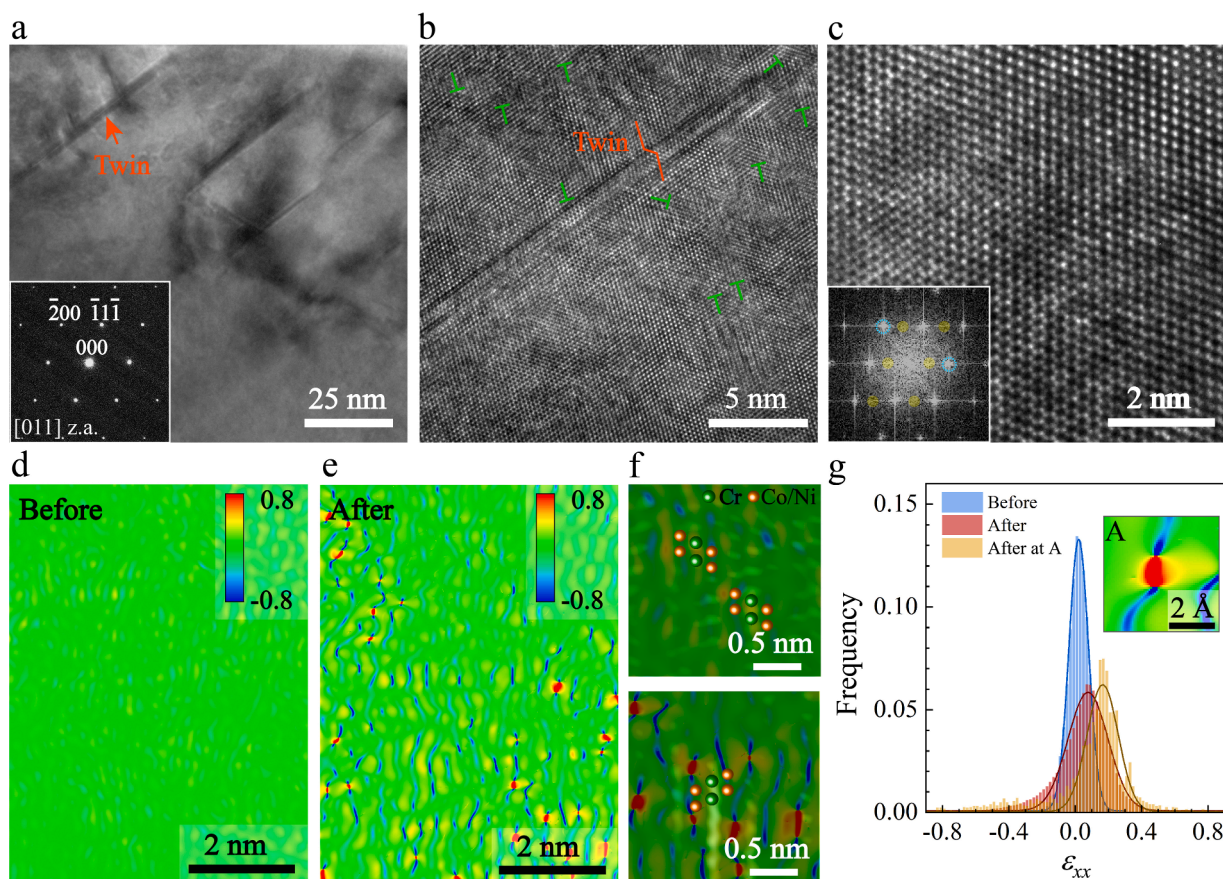

Fig. 11. (a)-(c) HRTEM images near the crack tip after deformation in the HS$_2$ sample. The inset in (a) shows the corresponding SAED pattern in the [011] zone axis. The inset in (c) is the corresponding FFT image (Blue circles: FCC diffraction spots. Yellow circles: extra superlattice scattering by CSROs). (d)(e) Strain maps before and after deformation, respectively. (f) Strain maps with IFFT lattice of CSROs before (first column, ε_{xx} ranges from -0.35 to 0.35) and after deformation (bottom column, ε_{xx} ranges from -0.8 to 0.8). (g) The distributions of ε_{xx} before and after deformation, in which region A is a local map of (e). (For interpretation of the references to color in this figure legend, the reader is referred to the web version of this article.)
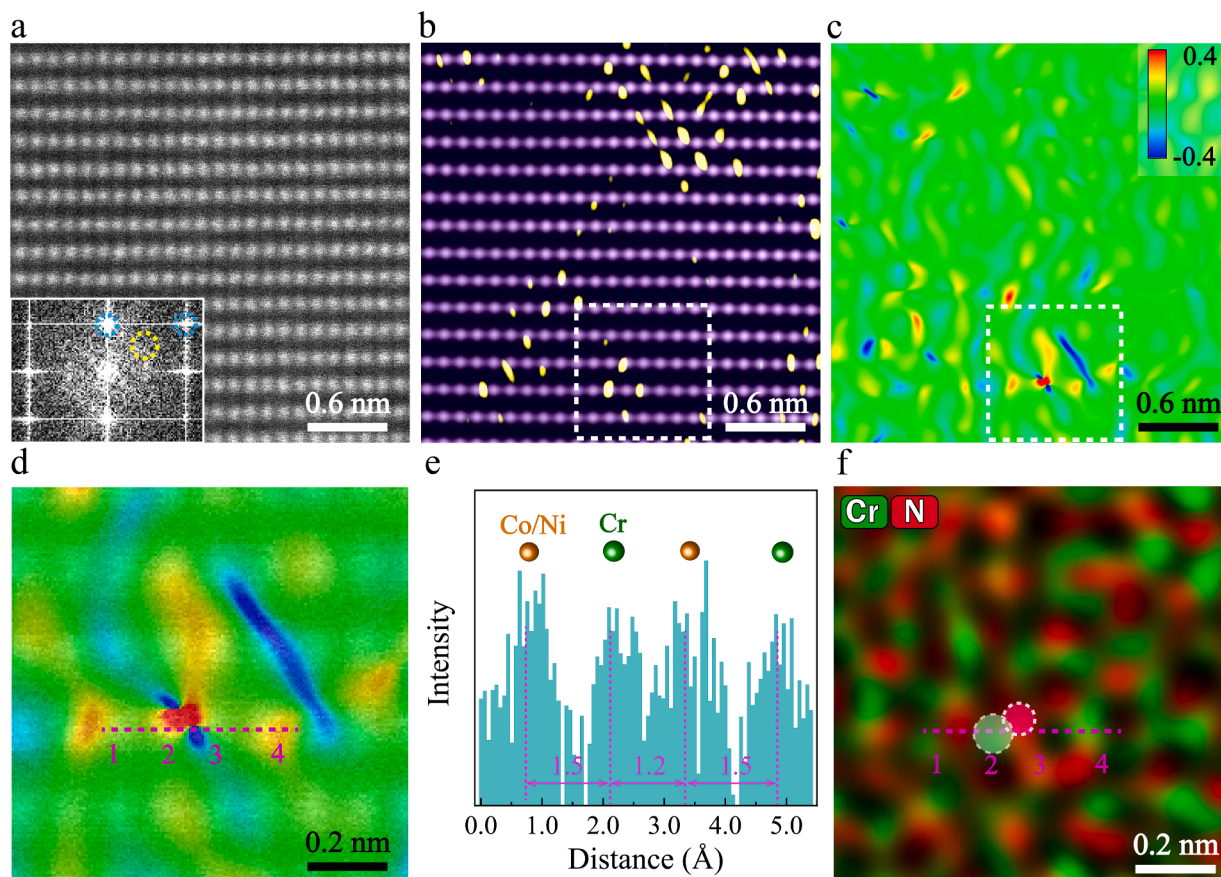
Fig. 12. Strain field analysis near CSROs after deformation for the HS$_2$ sample with the [112] zone axis. (a) HAADF image, the inset is the FFT image. Blue circles: FCC diffraction spots. Yellow circles: extra superlattice scattering by CSROs. (b) Overlapping the IFFT image of FCC matrix with CSROs. (c) GPA strain map after deformation. (d) Overlapping HAADF image on strain map in the rectangular box of (c). (e) The intensity distribution along the dashed line of (d). (f) EDS mapping of Cr and N elements. (For interpretation of the references to color in this figure legend, the reader is referred to the web version of this article.)

4.2. Crack propagation mechanism in HGS

The crack propagation and toughening mechanisms for the HS$_2$ sample with HGS are illustrated in Fig. 13. Three colors are used in the schematic diagram in Fig. 13 to distinguish MGs (light pink), UFGs (light green) and NGs (red). Cr$_2$N precipitates are marked in yellow. In the early stage (Fig. 13a), the crack does not extend and some plastic deformation is observed ahead of the crack tip. Even so, micro-voids already nucleate at the hard precipitates and the brittle interfaces between them and FCC matrix. With increasing applied stress, the crack tip is blunted significantly. In the plastic zone, severe plastic deformation provides intrinsic toughening ahead of the crack tip. As shown in Fig. 13b, abundant GNDs and SSDs are activated due to the

heterogeneous structure, CSRO/CMROs, and severe lattice distortion. Their interaction supports strong intrinsic toughening near the crack tip. In addition, grain refinement near the crack tip also provides extra hardening. In summary, these mechanisms provide crack tip hardening, and restrain crack propagation.

In addition to providing solid-solution hardening in the matrix, oversaturated nitrogen-atoms bonding with Cr-atoms form Cr$_2$N precipitates as well [46,51]. Ahead of crack tip, the micron-sized precipitates act as potential nucleation points for voids (Fig. 7). Number of micro-voids at the precipitates increases, such that localized deformation bands form along the main crack and adjacent micro-voids. These Cr$_2$N precipitates lead to early nucleation of micro-voids, which would reduce intrinsic toughness to some extent. Intrinsic toughening is
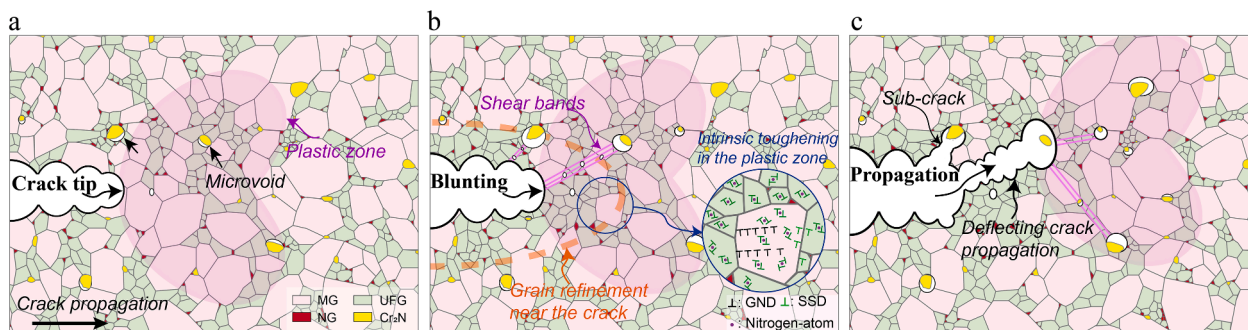

Fig. 13. Schematic diagram of the crack propagation and toughening mechanisms for the HS$_2$ sample with HGS. (a) Voids nucleate at the sites of Cr$_2$N precipitates. (b) Crack tip blunting and strain hardening behaviors at the plastic zone. (c) Crack propagation towards voids at the sites of Cr$_2$N precipitates.

important for the ductile metallic materials with low strength. While intrinsic toughening mechanisms become limited and the influence of extrinsic toughening becomes important for strong metals and alloys. The main crack converges with micro-voids and extends forward (Fig. 13c). Although these precipitates bear poor plastic deformation, and weaken the hardening of crack tip, they cause the reflection of crack propagation path when the main crack propagates toward adjacent micro-voids, considering that these precipitates are randomly distributed in the matrix. Moreover, some sub-cracks are also generated due to the existence of numerous micro-voids, which increases the energy dissipation during the main crack propagation. Therefore, besides the strain hardening near the crack tip, deflected crack path and additional crack branches can also provide extrinsic toughening to compensate for the loss of intrinsic toughness by precipitates. Both fraction and size of the Cr_2N precipitates in HS_1 and HS_2 are very similar, so precipitates should have a similar effect on fracture toughness of HS_1 and HS_2.

4.3. Effects of recrystallization degree on HDI hardening

In this research, two kinds of heterogeneous structures are investigated — HLS (HS_1) and HGS (HS_2). HS_1 is a partial recrystallized structure with ~54% of retained DGs after annealing (Fig. 2), while HS_2 is almost complete recrystallized (Fig. 3). HS_2 has a slightly lower σ_y (~ 1.0 GPa), but a much higher ε_u (~24%) than HS_1. HS_2 shows a much higher K_{IC} (~168 MPa·m$^{1/2}$) than HS_1(~91 MPa·m$^{1/2}$). Considering that the fraction and size of the Cr_2N precipitates in HS_1 and HS_2 are very similar, and the degree of CSROs increases with decreasing annealing temperature [15,22], thus a slightly higher proportion of CSROs and stronger effect on the fracture toughness could be inferred in HS_1. Since the HS_2 sample has a higher fracture toughness, it should be concluded that recrystallization degree plays a more important role in the difference of toughness between HS_1 and HS_2.

HS_1 sample has a greater heterogeneity than HS_2 sample due to significant strength difference between DGs and MGs. The statistical analysis of GNDs near the crack path is also conducted for HS_1 in Fig. S7a-c. The average increment of GND density ($\Delta\bar{\rho}_{GND}$) at the crack tip for recrystallization regions is calculated in Fig. S7d. HS_1 has a higher $\Delta\bar{\rho}_{GND}$ than HS_2 at HAGBs both in the UFGs and MGs, which indicates that HS_1 has a stronger HDI hardening than HS_2 at local hetero-interfaces. However, ~54% of deformed region is still reserved in the HS_1 sample. The distribution of DGs in HS_1 is more concentrated, thus the density of the hetero-interface (the length of hetero-interface per unit area) might be lower in HS_1. We measured the density of the hetero-interface between MGs and DGs/UFGs/NGs, the hetero-interface density is 0.44 μm length per μm^2 in HS_1 (according to Fig. 2b), while is 1.14 μm length per μm^2 in HS_2 (according to Fig. 3d). Therefore, more hetero-interfaces in HS_2 result in stronger HDI hardening at the macro scale. Moreover, HS_2 has a higher volume fraction of MGs than HS_1 prior to deformation, and dynamic grain refinement in MGs results in a HGS with even severer heterogeneity (Fig. S7e). Therefore, HS_2 has a more sustaining HDI hardening and a blunter crack tip than HS_1, which delays the crack propagation.

5. Conclusions

The fracture toughness of the CrCoNiN$_{1.75}$ MEA at different strength levels was investigated. The results reveal that the strategy of heterogeneous design is very effective on enhancing the yield strength and the fracture toughness in MEAs. The toughness mechanisms were analyzed, and several conclusions can be drawn as follows:

1) The heterogeneous structures show an improved strength-toughness synergy in the CrCoNiN$_{1.75}$ MEA with a yield strength of above 1.0 GPa. For HS_2 with HGS, a fracture toughness of 168 MPa·m$^{1/2}$ at a yield strength of about 1.0 GPa is observed. In comparison, for HS_1

with a HLS, a fracture toughness of 91 MPa·m$^{1/2}$ at a yield strength of almost 1.3 GPa is obtained.

2) The higher fracture toughness in the HS_2 sample can be attributed to the larger plastic zone size (r_c) and the higher hardening capacity (ΔHv) at the crack tip. Moreover, a positively linear relationship between J_{Hv} ($J_{Hv} = \int_0^{r_p} \Delta Hv dr$) and J_{IC} is established. Therefore, the quantitative relationship between the work hardening behavior of the crack tip and the fracture toughness is provided.

3) The superior fracture toughness in heterogeneous structure is related to the prominent HDI hardening. Strain incompatibility is observed between soft domains (MGs) and hard domains (NGs, UFGs or DGs), and GNDs generate near the interfaces to accommodate the strain gradient, which promotes additional HDI hardening at the plastic zone of the crack tip for higher fracture toughness. Meanwhile, dynamic grain refinement is observed near the crack path, which also provides extra hardening.

4) CSRO/CMROs stably exist before and after fracture tests. CSRO/CMROs can impede the motion of dislocations by interaction with moving dislocations, and thus improve hardening ability in the plastic zone.

5) The Cr_2N precipitates are potential nucleation sites for voids. These disorderly distributed precipitates ahead of the crack tip facilitate in deflecting crack path and induce crack branches, which provides extrinsic toughening to improve the fracture toughness. Our findings might promote the application of heterogeneous structures in other metals and alloys to achieve both high strength and high toughness.

CRediT authorship contribution statement

Xiaoru Liu: Conceptualization, Methodology, Validation, Formal analysis, Investigation, Writing – original draft, Writing – review & editing. **Shengde Zhang:** Methodology, Formal analysis, Investigation, Data curation, Writing – review & editing. **Hao Feng:** Methodology, Investigation, Resources, Writing – review & editing. **Jing Wang:** Investigation, Writing – review & editing. **Ping Jiang:** Investigation, Data curation, Supervision. **Huabing Li:** Resources, Supervision, Writing – review & editing. **Fuping Yuan:** Validation, Writing – review & editing, Visualization, Supervision. **Xiaolei Wu:** Validation, Writing – review & editing, Visualization, Supervision, Project administration.

Declaration of Competing Interest

The authors declare that they have no known competing financial interests or personal relationships that could have appeared to influence the work reported in this paper.

Supplementary materials

Supplementary material associated with this article can be found, in the online version, at doi:10.1016/j.actamat.2023.119079.

References

[1] Y.F. Ye, Q. Wang, J. Lu, C.T. Liu, Y. Yang, High-entropy alloy: challenges and prospects, Mater. Today 19 (2016) 349–362.
[2] D.B. Miracle, O.N. Senkov, A critical review of high entropy alloys and related concepts, Acta Mater 122 (2017) 448–511.
[3] E.P. George, D. Raabe, R.O. Ritchie, High-entropy alloys, Nat. Rev. Mater. 4 (2019) 515–534.

[4] E. Ma, X.L. Wu, Tailoring heterogeneities in high-entropy alloys to promote strength-ductility synergy, Nat. Commun. 10 (2019) 5623.

[5] E.P. George, W.A. Curtin, C.C. Tasan, High entropy alloys: A focused review of mechanical properties and deformation mechanisms, Acta Mater 188 (2020) 435–474.

[6] K.K. Ray, U. Roy, A. Ray, M. Kumari, A. Nath, Underlying mechanisms for deformation and fracture behaviour of some BCC and FCC high entropy alloys, Theor. Appl. Fract. Mech. 113 (2021).

[7] B. Gludovatz, A. Hohenwarter, D. Catoor, E.H. Chang, E.P. George, R.O. Ritchie, A fracture-resistant high-entropy alloy for cryogenic applications, Science 345 (2014) 1153–1158.

[8] B. Gludovatz, A. Hohenwarter, K.V. Thurston, H. Bei, Z. Wu, E.P. George, R. O. Ritchie, Exceptional damage-tolerance of a medium-entropy alloy CrCoNi at cryogenic temperatures, Nat. Commun. 7 (2016) 10602.

[9] Z. Zhang, M.M. Mao, J. Wang, B. Gludovatz, Z. Zhang, S.X. Mao, E.P. George, Q. Yu, R.O. Ritchie, Nanoscale origins of the damage tolerance of the high-entropy alloy CrMnFeCoNi, Nat. Commun. 6 (2015) 10143.

[10] Z. Zhang, H. Sheng, Z. Wang, B. Gludovatz, Z. Zhang, E.P. George, Q. Yu, S.X. Mao, R.O. Ritchie, Dislocation mechanisms and 3D twin architectures generate exceptional strength-ductility-toughness combination in CrCoNi medium-entropy alloy, Nat. Commun. 8 (2017) 14390.

[11] Q.Q. Ding, X.Q. Fu, D.K. Chen, H.B. Bei, B. Gludovatz, J.X. Li, Z. Zhang, E. P. George, Q. Yu, T. Zhu, R.O. Ritchie, Real-time nanoscale observation of deformation mechanisms in CrCoNi-based medium- to high-entropy alloys at cryogenic temperatures, Mater. Today 25 (2019) 21–27.

[12] G. Laplanche, A. Kostka, C. Reinhart, J. Hunfeld, G. Eggeler, E.P. George, Reasons for the superior mechanical properties of medium-entropy CrCoNi compared to high-entropy CrMnFeCoNi, Acta Mater 128 (2017) 292–303.

[13] J. Miao, C.E. Slone, T.M. Smith, C. Niu, H. Bei, M. Ghazisaeidi, G.M. Pharr, M. J. Mills, The evolution of the deformation substructure in a Ni-Co-Cr equiatomic solid solution alloy, Acta Mater 132 (2017) 35–48.

[14] F. Otto, A. Dlouhý, C. Somsen, H. Bei, G. Eggeler, E.P. George, The influences of temperature and microstructure on the tensile properties of a CoCrFeMnNi high-entropy alloy, Acta Mater 61 (2013) 5743–5755.

[15] Q.J. Li, H. Sheng, E. Ma, Strengthening in multi-principal element alloys with local-chemical-order roughened dislocation pathways, Nat. Commun. 10 (2019) 3563.

[16] E. Ma, Unusual dislocation behavior in high-entropy alloys, Scr. Mater. 181 (2020) 127–133.

[17] J.B. Seol, J.W. Bae, J.G. Kim, H. Sung, Z. Li, H.H. Lee, S.H. Shim, J.H. Jang, W.-S. Ko, S.I. Hong, H.S. Kim, Short-range order strengthening in boron-doped high-entropy alloys for cryogenic applications, Acta Mater 194 (2020) 366–377.

[18] X.F. Chen, Q. Wang, Z.Y. Cheng, M.L. Zhu, H. Zhou, P. Jiang, L.L. Zhou, Q.Q. Xue, F.P. Yuan, J. Zhu, X.L. Wu, E. Ma, Direct observation of chemical short-range order in a medium-entropy alloy, Nature 592 (2021) 712–716.

[19] D. Liu, Q. Wang, J. Wang, X.F. Chen, P. Jiang, F.P. Yuan, Z.Y. Cheng, E. Ma, X. L. Wu, Chemical short-range order in Fe50Mn30Co10Cr10 high-entropy alloy, Mater. Today Nano 16 (2021), 100139.

[20] J. Wang, P. Jiang, F.P. Yuan, X.L. Wu, Chemical medium-range order in a medium-entropy alloy, Nat. Commun. 13 (2022) 1021.

[21] X.F. Yang, Y.Z. Xi, C.Y. He, H. Chen, X.C. Zhang, S.T. Tu, Chemical short-range order strengthening mechanism in CoCrNi medium-entropy alloy under nanoindentation, Scr. Mater. 209 (2022), 114364.

[22] L.L. Zhou, Q. Wang, J. Wang, X.F. Chen, P. Jiang, H. Zhou, F.P. Yuan, X.L. Wu, Z. Y. Cheng, E. Ma, Atomic-scale evidence of chemical short-range order in CrCoNi medium-entropy alloy, Acta Mater 224 (2022), 117490.

[23] M.E. Launey, R.O. Ritchie, On the Fracture Toughness of Advanced Materials, Adv. Mater. 21 (2009) 2103–2110.

[24] K. Lu, The Future of Metals, Mater. Sci. 328 (2010) 319–320.

[25] R.O. Ritchie, The conflicts between strength and toughness, Nat. Mater. 10 (2011) 817–822.

[26] K. Lu, Making strong nanomaterials ductile with gradients, Science 345 (2014) 1455–1456.

[27] X.L. Wu, P. Jiang, L. Chen, F.P. Yuan, Y.T. Zhu, Extraordinary strain hardening by gradient structure, Proc. Natl. Acad. Sci. U.S.A. 111 (2014) 7197–7201.

[28] S. Qin, M.X. Yang, P. Jiang, J. Wang, X.L. Wu, H. Zhou, F.P. Yuan, Designing structures with combined gradients of grain size and precipitation in high entropy alloys for simultaneous improvement of strength and ductility, Acta Mater 230 (2022), 117847.

[29] X.L. Wu, M.X. Yang, F.P. Yuan, L. Chen, Y.T. Zhu, Combining gradient structure and TRIP effect to produce austenite stainless steel with high strength and ductility, Acta Mater 112 (2016) 337–346.

[30] Z. Cheng, H.F. Zhou, Q.H. Lu, H.J. Gao, L. Lu, Extra strengthening and work hardening in gradient nanotwinned metals, Science 362 (2018) eaau1925.

[31] X.L. Wu, M.X. Yang, F.P. Yuan, G.L. Wu, Y.J. Wei, X.X. Huang, Y.T. Zhu, Heterogeneous lamella structure unites ultrafine-grain strength with coarse-grain ductility, Proc. Natl. Acad. Sci. U.S.A. 112 (2015) 14501–14505.

[32] S.D. Zhang, M.X. Yang, F.P. Yuan, L.L. Zhou, X.L. Wu, Extraordinary fracture toughness in nickel induced by heterogeneous grain structure, Mater. Sci. Eng. A 830 (2022), 142313.

[33] G. Niu, H.S. Zurob, R.D.K. Misra, Q.B. Tang, Z.H. Zhang, M.T. Nguyen, L.L. Wang, H.B. Wu, Y. Zou, Superior fracture toughness in a high-strength austenitic steel with heterogeneous lamellar microstructure, Acta Mater 226 (2022), 117642.

[34] M.X. Yang, D.S. Yan, F.P. Yuan, P. Jiang, E. Ma, X.L. Wu, Dynamically reinforced heterogeneous grain structure prolongs ductility in a medium-entropy alloy with gigapascal yield strength, Proc. Natl. Acad. Sci. U.S.A. 115 (2018) 7224–7229.

[35] E. Ma, T. Zhu, Towards strength-ductility synergy through the design of heterogeneous nanostructures in metals, Mater. Today 20 (2017) 323–331.

[36] X.L. Wu, Y.T. Zhu, Heterogeneous materials: a new class of materials with unprecedented mechanical properties, Mater. Res. Lett. 5 (2017) 527–532.

[37] X.L. Wu, Y.T. Zhu, Gradient and lamellar heterostructures for superior mechanical properties, MRS Bull. 46 (2021) 244–249.

[38] L. Xiong, Z.S. You, S.D. Qu, L. Lu, Fracture behavior of heterogeneous nanostructured 316L austenitic stainless steel with nanotwin bundles, Acta Mater 150 (2018) 130–138.

[39] H.Z. Zhao, Z.S. You, N.R. Tao, L. Lu, Anisotropic toughening of nanotwin bundles in the heterogeneous nanostructured Cu, Acta Mater 228 (2022).

[40] L. Liu, Q. Yu, Z. Wang, J. Ell, M.X. Huang, R.O. Ritchie, Making ultrastrong steel tough by grain-boundary delamination, Science 368 (2020) 1347–1352.

[41] Q.Q. Ding, Y. Zhang, X. Chen, X.Q. Fu, D.K. Chen, S.J. Chen, L. Gu, F. Wei, H.B. Bei, Y.F. Gao, M.R. Wen, J.X. Li, Z. Zhang, T. Zhu, R.O. Ritchie, Q. Yu, Tuning element distribution, structure and properties by composition in high-entropy alloys, Nature 574 (2019) 223–227.

[42] S. Chen, Z.H. Aitken, S. Pattamatta, Z. Wu, Z.G. Yu, D.J. Srolovitz, P.K. Liaw, Y. W. Zhang, Simultaneously enhancing the ultimate strength and ductility of high-entropy alloys via short-range ordering, Nat. Commun. 12 (2021) 4953.

[43] A. Abu-Odeh, M. Asta, Modeling the effect of short-range order on cross-slip in an FCC solid solution, Acta Mater 226 (2022), 117615.

[44] J.Y. Ko, S.I. Hong, Microstructural evolution and mechanical performance of carbon-containing CoCrFeMnNi-C high entropy alloys, J. Alloys Compd. 743 (2018) 115–125.

[45] E.G. Astafurova, K.A. Reunova, E.V. Melnikov, M.Y. Panchenko, S.V. Astafurov, G. G. Maier, V.A. Moskvina, On the difference in carbon- and nitrogen-alloying of equiatomic FeMnCrNiCo high-entropy alloy, Mater. Lett. 276 (2020), 128183.

[46] D.E. Jodi, N. Choi, J. Park, N. Park, Mechanical Performance Improvement by Nitrogen Addition in N-CoCrNi Compositionally Complex Alloys, Metall. Mater. Trans. A 51 (2020) 3228–3237.

[47] M. Klimova, D. Shaysultanov, A. Semenyuk, S. Zherebtsov, G. Salishchev, N. Stepanov, Effect of nitrogen on mechanical properties of CoCrFeMnNi high entropy alloy at room and cryogenic temperatures, J. Alloys Compd. 849 (2020), 156633.

[48] Y. Han, H.B. Li, H. Feng, Y.Z. Tian, Z.H. Jiang, T. He, Mechanism of dislocation evolution during plastic deformation of nitrogen-doped CoCrFeMnNi high-entropy alloy, Mater. Sci. Eng. A 814 (2021), 141235.

[49] A. Semenyuk, M. Klimova, D. Shaysultanov, G. Salishchev, S. Zherebtsov, N. Stepanov, Effect of nitrogen on microstructure and mechanical properties of the CoCrFeMnNi high-entropy alloy after cold rolling and subsequent annealing, J. Alloys Compd. 888 (2021), 161452.

[50] M. Traversier, P. Mestre-Rinn, N. Peillon, E. Rigal, X. Boulnat, F. Tancret, J. Dhers, A. Fraczkiewicz, Nitrogen-induced hardening in an austenitic CrFeMnNi high-entropy alloy (HEA), Mater. Sci. Eng. A 804 (2021), 140725.

[51] J. Zhang, K.N. Yoon, M.S. Kim, H.S. Ahn, J.Y. Kim, Z.H. Li, T. Sasaki, K. Hono, E. S. Park, Strengthening by customizing microstructural complexity in nitrogen interstitial CoCrFeMnNi high-entropy alloys, J. Alloys Compd. 901 (2022), 163483.

[52] ASTME1820-18, Standard Test Method for Measurement of Fracture Toughness, American Society for Testing and Materials, Philadelphia (PA), 2018.

[53] P.J. Konijnenberg, S. Zaefferer, D. Raabe, Assessment of geometrically necessary dislocation levels derived by 3D EBSD, Acta Mater 99 (2015) 402–414.

[54] Y.H. Jo, K.-Y. Doh, D.G. Kim, K. Lee, D.W. Kim, H. Sung, S.S. Sohn, D. Lee, H. S. Kim, B.-J. Lee, S. Lee, Cryogenic-temperature fracture toughness analysis of non-equi-atomic V10Cr10Fe45Co20Ni15 high-entropy alloy, J. Alloys Compd. 809 (2019), 151864.

[55] Y.H. Jo, J. Yang, K.-Y. Doh, W. An, D.W. Kim, H. Sung, D. Lee, H.S. Kim, S.S. Sohn, S. Lee, Analysis of damage-tolerance of TRIP-assisted V10Cr10Fe45Co30Ni5 high-entropy alloy at room and cryogenic temperatures, J. Alloys Compd. 844 (2020), 156090.

[56] C. Chen, S.J. Pang, Y.Y. Cheng, T. Zhang, Microstructure and mechanical properties of Al20−xCr20+0.5xFe20Co20Ni20+0.5x high entropy alloys, J. Alloys Compd. 659 (2016) 279–287.

[57] M. Seifi, D.Y. Li, Z. Yong, P.K. Liaw, J.J. Lewandowski, Fracture Toughness and Fatigue Crack Growth Behavior of As-Cast High-Entropy Alloys, JOM 67 (2015) 2288–2295.

[58] A.J. Zhang, J.S. Han, J.H. Meng, B. Su, P.D. Li, Rapid preparation of AlCoCrFeNi high entropy alloy by spark plasma sintering from elemental powder mixture, Mater. Lett. 181 (2016) 82–85.

[59] S.P. Wang, E. Ma, J. Xu, Notch fracture toughness of body-centered-cubic (TiZrNbTa)-Mo high entropy alloys, Intermetallics 103 (2018) 78–87.

[60] U. Roy, H. Roy, H. Daoud, U. Glatzel, K.K. Ray, Fracture toughness and fracture micromechanism in a cast AlCoCrCuFeNi high entropy alloy system, Mater. Lett. 132 (2014) 186–189.

[61] J.E. Pawel, D.J. Alexander, M.L. Grossbeck, A.W. Longest, A.F. Rowcliffe, G. E. Lucas, S. Jitsukawa, A. Hishinuma, K. Shiba, Fracture toughness of candidate materials for ITER first wall, blanket, and shield structures, J. Nucl. Mater. 212-215 (1994) 442–447.

[62] W.J. Mills, Fracture toughness of type 304 and 316 stainless steels and their welds, Int. Mater. Rev. 42 (1997) 45–82.

[63] G. Sasikala, S.K. Ray, Influence of ageing on the quasistatic fracture toughness of an SS 316(N) weld at ambient and elevated temperatures, J. Nucl. Mater. 408 (2011) 45–53.

[64] J. Kobayashi, D. Ina, A. Futamura, K. Sugimoto, Fracture Toughness of an Advanced Ultrahigh-strength TRIP-aided Steel, ISIJ Int 54 (2014) 955–962.

[65] R. Eckner, L. Krüger, C. Ullrich, M. Wendler, O. Volkova, Fracture toughness of high-alloy austenitic-martensitic TRIP steels after Q&P processing, Int. J. Fract. 215 (2019) 139–151.

[66] R.Q. Cao, Q. Yu, J. Pan, Y. Lin, A. Sweet, Y. Li, R.O. Ritchie, On the exceptional damage-tolerance of gradient metallic materials, Mater. Today 32 (2020) 94–107.

[67] S.K. Putatunda, Fracture toughness of a high carbon and high silicon steel, Mater. Sci. Eng. A 297 (2001) 31–43.

[68] X.R. Liu, H. Feng, J. Wang, X.F. Chen, P. Jiang, F.P. Yuan, H.B. Li, E. Ma, X.L. Wu, Mechanical property comparisons between CrCoNi medium-entropy alloy and 316 stainless steels, J. Mater. Sci. Technol. 108 (2022) 256–269.

[69] M.J. Hÿtch, E. Snoeck, R. Kilaas, Quantitative measurement of displacement and strain fields from HREM micrographs, Ultramicroscopy 74 (1998) 131–146.

[70] X.F. Chen, F.P. Yuan, H. Zhou, X.L. Wu, Structure motif of chemical short-range order in a medium-entropy alloy, Mater. Res. Lett. 10 (2022) 149–155.

[71] R. Zhang, S. Zhao, J. Ding, Y. Chong, T. Jia, C. Ophus, M. Asta, R.O. Ritchie, A. M. Minor, Short-range order and its impact on the CrCoNi medium-entropy alloy, Nature 581 (2020) 283–287.

[72] Y. Ma, F.P. Yuan, M.X. Yang, P. Jiang, E. Ma, X.L. Wu, Dynamic shear deformation of a CrCoNi medium-entropy alloy with heterogeneous grain structures, Acta Mater 148 (2018) 407–418.